NEAR-INFRARED IMAGING AND [O I] SPECTROSCOPY OF IC 443 USING TWO MICRON ALL SKY SURVEY AND *INFRARED SPACE OBSERVATORY*

JEONGHEE RHO, T. H. JARRETT, R. M. CUTRI, AND W. T. REACH

Infrared Processing and Analysis Center, California Institute of Technology, MS 100-22, Pasadena, CA 91125

Received 2000 March 28; accepted 2000 September 28

ABSTRACT

We present near-infrared J (1.25 μm), H (1.65 μm), and K_s (2.17 μm) imaging of the entire supernova remnant IC 443 from the Two Micron All Sky Survey (2MASS), and *Infrared Space Observatory* (*ISO*) LWS observations of [O I] for 11 positions in the northeast. Near-infrared emission from IC 443 was detected in all three bands from most of the optically bright parts of the remnant, revealing a shell-like morphology, with bright K_s-band emission along the southern ridge and bright J and H along the northeastern rim. The total luminosity within the 2MASS bands is 1.3×10^{36} ergs s^{-1}. These data represent the first near-infrared images that are complete in coverage of the remnant.

The color and morphological structure are very different between the northeastern and southern parts. J- and H-band emission from the northeast rim is comparably bright and can be explained mostly by [Fe II] line emission. The hydrogen recombination lines, Pβ and Br10, should also be present in the broadband images, but probably contribute less than 10% of the J- and H-band fluxes. Strong [O I] (63 μm) lines were detected crossing the northeastern rim, with the strongest line in the northeastern shell where the near-infrared emission shows filamentary structure. In contrast, the southern ridge is dominated by K_s-band light exhibiting a clumped and knotty structure. A two excitation temperature model derived from previous *ISO* and ground-based observations predicts that H_2 lines can explain most of K_s band and at least half of J- and H-band emission. Hence, the prominent broadband color differences arise from physically different mechanisms: atomic fine structure lines along the northeastern rim and molecular rovibrational lines along the southern ridge. Shock models imply a fast J-shock with $v_s \sim 100$ km s^{-1} and $10 < n_o < 10^3$ cm^{-3} for the northeastern rim and a slow C-shock with $v_s \sim 30$ km s^{-1} and $n_o \sim 10^4$ cm^{-3} for the southern ridge, respectively.

The shocked H_2 line emission is well known from the southern sinuous ridge, produced by an interaction with dense molecular clouds. The large field of view and color of the 2MASS images show that the K_s-band emission extends to the east and the northeast, suggesting that the interaction extends to the inner part of the northeastern shell. Our new CO map of the inner part of the northeast quadrant shows good correspondence with the K_s-band map. The CO lines are broad, confirming that the K_s-band emission is due to shocked H_2.

Subject headings: infrared: ISM: lines and bands — ISM: individual (IC 443) — supernova remnants

1. INTRODUCTION

IC 443 is the best-studied case of supernova remnant–molecular cloud interaction. The system is observed to have broad molecular lines with CO gas accelerated to 20 km s^{-1} and shocked H_2 emission along the southern ridge (van Dishoeck et al. 1993; Burton et al. 1988). The molecular cloud stretches across the remnant from the north to the south as projected along the line of sight (Cornett, Chin, & Knapp 1977). IC 443 is in the Gem OB 1 association, located close to the Galactic plane (G189.1 + 3.0). Optical spectroscopy of the northeastern filaments of IC 443 indicated a shock velocity of $v_s \sim 65$–100 km s^{-1} and a preshock density of $n_o \sim 10$–20 cm^{-3} (Fesen & Kirshner 1980). Shocked H I is associated with the bright northeastern filaments and extends across the entire southern hemisphere of the remnant with velocities up to 100 km s^{-1} (Giovanelli & Haynes 1979). IC 443 has unusual morphology; the optical and radio morphology is shell-like, but it extends eastward beyond the main shell (referred to the "northeastern arm"). The optical emission shows radial filaments with different curvature in the southwest, and the X-ray emission appears both at the interior of the shell and at the edge of the shell (Petre et al. 1988; Rho, Petre, & Hester 1993). A superposition with another SNR G189.6 + 3.3 has been suggested (Asaoka & Aschenbach 1994).

The presence of H_2 line emission along the southern ridge strongly suggests that the supernova shock wave is interacting with the molecular cloud (Burton et al. 1988; Richter et al. 1995). A near-infrared line of [Fe II] (1.64 μm) is detected from the northeastern shell, 30 times as strong as that of Brγ, which is much stronger than seen in Galactic H II regions. The strong [Fe II] line is produced not only by efficient excitation of Fe but also by grain destruction (Graham, Wright, & Longmore 1987).

Infrared emission from supernova remnants, including IC 443, is not well understood. *IRAS* observations show bright emission from IC 443, which was interpreted as thermal continuum emission from heated small and large dust grains (Arendt 1989; Saken, Fesen, & Shull 1992; Braun & Strom 1986). However, recent *Infrared Space Observatory* (*ISO*) observations show no continuum between 5–14 μm with a noise level of 0.2×10^{-4} ergs s^{-1} cm^{-2} sr^{-1} (Cesarsky et al. 1999). Instead, the observed mid-infrared spectrum of the shocked gas is dominated by rich emission lines of H_2. *ISO* SWS observations of the northeastern filaments (Oliva et al. 1999a) also showed detections of rich emission lines, not molecular but ionic lines such as [Ne II], [Fe II], and [Si II]. Previous interpretations of the *IRAS* 12 and 25 μm emission are different, based on differences between the *ISO* SWS and ISOCAM results. In particular,

Oliva et al. (1999a) suggested that 25 μm *IRAS* emission is virtually all ionized ion lines, while Cesarsky et al (1999) claimed that shocked H_2 lines (at least at the southern region) are dominant. This is due to limited field of view of *ISO* observations toward IC 443, and also due to limited spatial resolution of the *IRAS* image.

In this paper, we present *J*, *H*, and K_s imaging from the Two Micron All Sky Survey (2MASS, Skrutskie et al. 1997) covering the entire size of the IC 443 remnant, and we show which spectral lines contribute to the *J*-, *H*-, and K_s-band emission. We present detections of the [O I] 63 μm line using *ISO* LWS observations. Combining the 2MASS and *ISO* data, we employ diagnostics for rating the cooling in atomic or molecular shocks and compare the line brightnesses with J- and C-shock models.

While previous near-infrared imaging and spectroscopic observations were limited to a part of the supernova remnant, the 2MASS image offers a global view of the emission, and it provides a means to understand the surrounding ISM environment. IC 443 is the first such example, and we expect other supernova remnants will be revealed in the near-infrared light using 2MASS.

2. OBSERVATION

2.1. *Two Micron All Sky Survey*

Using identical telescopes in the northern and southern hemispheres, 2MASS is mapping the entire sky in the *J* (1.11–1.36 μm), *H* (1.5–1.8 μm), and K_s (2–2.32 μm) bands to a limiting point source sensitivity of approximately 16.5, 16.0, and 15.5 mag, respectively. 2MASS observed IC 443 on 1997 November 23 UT using the northern telescope at Mt. Hopkins, Arizona. The data are acquired in $8.5 \times 6°$ "tiles" for net 7.8 s exposures of each point on the sky, and pipeline data processing produces calibrated $8.5 \times 17'$ Atlas Images in the three survey bands.[1] The image resolution is typically 3.5, twice the camera resolution, and the data are sampled with 1" per pixel.

A total of twenty-four 2MASS Atlas Images in each band covering the $1° \times 1°$ region around IC 443 were combined to produce the large mosaic shown in Figure 1. The mosaic was constructed by first combining in the declination direction the three Atlas Images (per band) that fall in the same

[1] See R. M.Cutri et al. at http://www.ipac.caltech.edu/2mass/releases/first/doc/explsup.html.

2MASS tile into individual strips. Eight such strips were formed in each band. The low-frequency atmospheric emission gradients in each 2MASS "tile" were then fit out, using a 17' median filter in the declination direction. This background subtraction does not affect the nebular emission scales with which this work is concerned, and any large-scale ($>17'$) emission of the SNR is obscured by the low-frequency atmospheric emission gradients. The background levels in each pixel of the eight strips were then adjusted using the intensity offsets in the approximately 1' R.A. overlap region between tiles. Surface brightness profiles in Figure 2 show the resultant background fluctuation in the right ascension direction, and the average surface brightnesses over a 1 arcmin^2 area for a representative position from the northeastern rim for *J* and *H* bands and from the southern ridge for K_s band are also shown.

The 2MASS flux calibrations for each band were 7.46×10^{-6} Jy DN^{-1}, 5.75×10^{-6} Jy DN^{-1} and 7.12×10^{-6} Jy DN^{-1}, for *J*, *H*, and K_s, respectively. These values are derived using the zero-point flux of 1603, 1075, and 698 Jy, and the average zero-point magnitudes (background) are 20.83, 20.68, and 20.0 mag, for *J*, *H*, and K_s, respectively. The current absolute zero-point fluxes of 2MASS have an estimated 5% uncertainty. The filter FWHM passbands are 0.25, 0.3, and 0.32 μm, *J*, *H*, and K_s, respectively, where the long-wavelength cutoff in *J* band is defined by atmospheric H_2O and CO_2 absorption. The central wavelengths of 1.25, 1.65, and 2.17 μm, for *J*, *H*, and K_s, respectively, are used. The unit DN is equivalent to 1.52×10^{-4}, 0.83×10^{-4}, and 0.61×10^{-4} ergs s^{-1} cm^{-2} sr^{-1}, for the *J*, *H*, and K_s bands, respectively, which are used to estimate the surface brightness shown in Table 1.

2.2. *2MASS Near-Infrared Images*

Emission from IC 443 was detected in all three bands from most of the optically bright parts of the remnant, revealing a shell-like morphology. The K_s-band image also shows bright emission at the southern ridge. These are the first near-infrared images that cover the entire remnant. Figure 1 shows the combined *J*, *H*, and K_s mosaic image, with *J* assigned to blue, *H* to green and K_s to red color. The surface brightness in Figure 1 ranges from (0.3–6.4), (0.2–4.0), (0.1–12) with units of 10^{-4} ergs s^{-1} cm^{-2} sr^{-1} for the *J*, *H*, and K_s bands, respectively. The color and structure are in sharp contrast between the northeastern and southern

TABLE 1

MEASURED IN-BAND SURFACE BRIGHTNESSES USING 2MASS IMAGES

Band	*J*	*H*	K_s	$J:H:K_s$
Northeastern Rim (position 1)				
Flux	2.28 ± 0.30	1.58 ± 0.39	0.28 ± 0.26	1:0.7:0.1
Unred	4.49 ± 0.60	2.40 ± 0.60	0.37 ± 0.34	1:0.5:0.08
NE Front				
Flux	0.06 ± 0.05	0.10 ± 0.09	0.30 ± 0.10	0.2:0.3:1
Unred	0.12 ± 0.11	0.15 ± 0.14	0.40 ± 0.13	0.3:0.37:1
East				
Flux	0.73 ± 0.18	1.19 ± 0.43	0.81 ± 0.15	1:1.6:1.1
Unred	1.62 ± 0.4	1.95 ± 0.71	1.12 ± 0.21	1:1.2:0.7
South (clump G)				
Flux	0.80 ± 0.23	0.87 ± 0.28	2.44 ± 0.18	0.33:0.36:1
Unred	1.88 ± 0.54	1.48 ± 0.48	3.44 ± 0.25	0.5:0.4:1

The surface brightnesses have units of 10^{-4} ergs s^{-1} cm^{-2} sr^{-1}. "Unred" indicates the extinction corrected brightness.

FIG. 1.—Mosaiced 2MASS Atlas Image of IC 443. *J*, *H*, and K_s images show color contrast between northeastern rim (*J and H emission is shown with blue and green, respectively*) and southern ridge (K_s *emission is shown with red*). The northeastern rim is dominated by [Fe II] and Pβ (J) and [Fe II] (H), while southern sinuous ridge emission is mostly H_2 lines.
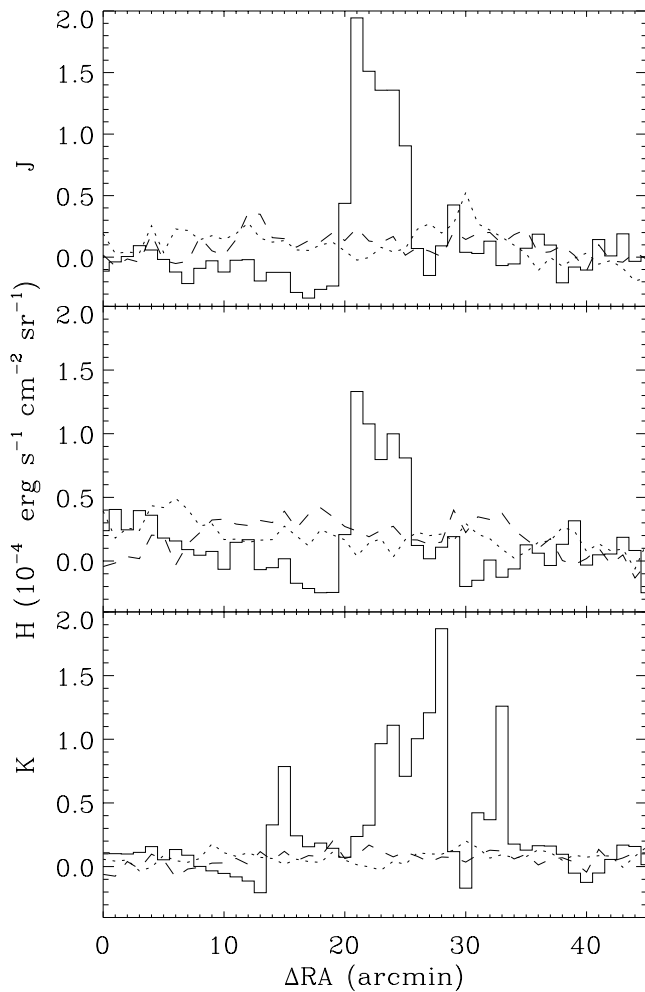
FIG. 2.—Surface brightness profile across the R.A. direction after the images are mosaiced for (a) J, (b) H, and (c) K_s bands, respectively. The dotted lines are backgrounds at the northern portion and at the southern portion of the mosaiced image, and the solid lines for J and H are crossing decl. $22°52'55''$ (J2000), and for K_s, crossing the position of decl. $22°25'24''$ (J2000).

parts. While the northeastern rim is dominated by J- and H- band emission (represented with blue and green colors in Fig. 1), the southern ridge is dominated by K_s band emission (red in Fig. 1). The K_s-band emission defining the southern ridge is remarkably the same as those H_2 maps (2.2 μm) in Burton et al. (1988) and Richter et al. (1995), except that the 2MASS mosaic covers a larger field. The J and H emission represents the first near-infrared imaging of IC 443. Figures 3a–3c show the mosaiced image after removing stars using DAOPHOT. Removal of the stars was necessary to estimate the surface brightnesses shown in Table 1 because a small contribution from faint stars would easily cause overestimation of the remnant flux.

We divided IC 443 into two global fields—the northeastern rim and the southern ridge—in order to compare and contrast the detailed line diagnostics and physical parameters between fields. We have measured the surface brightnesses of the images for a number of positions, verifying that the apparent color contrast between the northeast and southern fields is real (see Table 1). For the northeastern position we used "position 1" (R.A. $06^h17^m34^s41$ and decl. $+22° 52'55''2$ [epoch J2000]), where the inten-

sities of [Fe II] lines were measured by Graham et al. (1987). Here the targeted region is defined by an ellipse with a radius of $48'' \times 18''$ and a position angle of $300°$ (east of north). The southern position (R.A. $06^h16^m42^s40$, decl. $+22°32'4''0$) is where ISOCAM observations were carried out (clump G of Cesarsky et al. 1999). The targeted region is $37'' \times 69''$ with an angle of $70°$. Measured mean surface brightnesses are given in Table 1. The "position 1" and "south (clump G)" positions are marked in Figure 3b. The $J:H:K_s$ ratio represents the southern sinuous ridge in the K_s-band–dominated area (red in Fig. 1). In the K_s-band–dominated area, the eastern side of IC 443 shows different $J:H:K_s$ ratio from those in the southern sinuous ridge. The southern sinuous ridge within which the $J:H:K_s$ ratio is similar to that of "south (clump G)" defines below decl. $+22°30'00''$ in the eastern side as well as the south. The position "east" in Table 1 (see Fig. 3b) shows brighter emission in J and H (relative to K_s) when compared with that of the southern sinuous ridge region. The estimated surface brightnesses in Table 1 have $\sim 30\%$ uncertainty due to real surface brightness variation within the elliptical regions.

We have measured J-, H-, and K_s-band surface brightnesses from a few extra positions. Within the northeastern rim (blue and green in Fig. 1) the $J:H:K_s$ brightness ratios are similar to that of "position 1" with less than 10% variation. However, the K_s-dominated area (red in Fig. 1) is subdivided into two area. One is the southern sinuous ridge and the other is the eastern part of the remnant. Within the southern sinuous ridge (including the clump G position in the southwest), the $J:H:K_s$ brightness ratios are also similar to that of the "south" (clump G) position with less than 10% variation. However, in the eastern part, the $J:H:K_s$ ratio gradually changes position by position from the ratio of southern ridge to the ratio of northeastern rim.

The possible emission sources that contribute to the 2MASS near-infrared emission include hydrogen recombination (Pβ, Br10, and Brγ), molecular hydrogen lines [e.g., 2-0 S(1), 1-0 S(7) and 1-0 S(1)] and forbidden ionic lines (e.g. [Fe II]). We assume there is negligible continuum within the 2MASS bands because the *ISO* observations show no continuum for 5–14 μm. The noise level of the ISOCAM observation was 0.2×10^{-4} ergs s^{-1} cm^{-2} sr^{-1}, which is comparable to the errors of 2MASS measurements in Table 1, and the near-infrared continuum brightness is expected to be smaller than that of mid-infrared from heated small grains if they survived the shock (Dwek & Arendt 1992). If there is continuum, it would be less than 10% of the 2MASS surface brightnesses. Moreover, previously measured line fluxes of [Fe II] and H_2 were comparable to those of J, H, and K bands within errors (see details in §§ 3 and 4). The estimated nonthermal continuum due to synchrotron radiation, likewise, is too small to contribute to the 2MASS observed brightness.

2.3. *ISO*

ISO LWS observations of [O I] (63.2 μm) were carried out for 11 positions of the northeast field, crossing the northeastern rim with an interval of $160''$ (illustrated in Fig. 3b on the H-band image). The beam size is $80''$. The observations took place 1998 February 27 UT. The total time for these observations was 19 minutes, with approximately 1 minute dedicated to each spectrum. We averaged the individual scans and fit the detected lines with gaussians. The
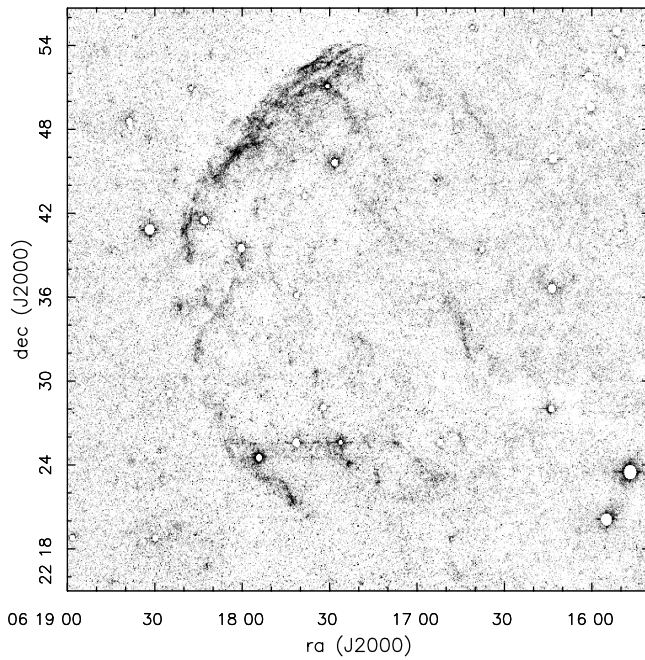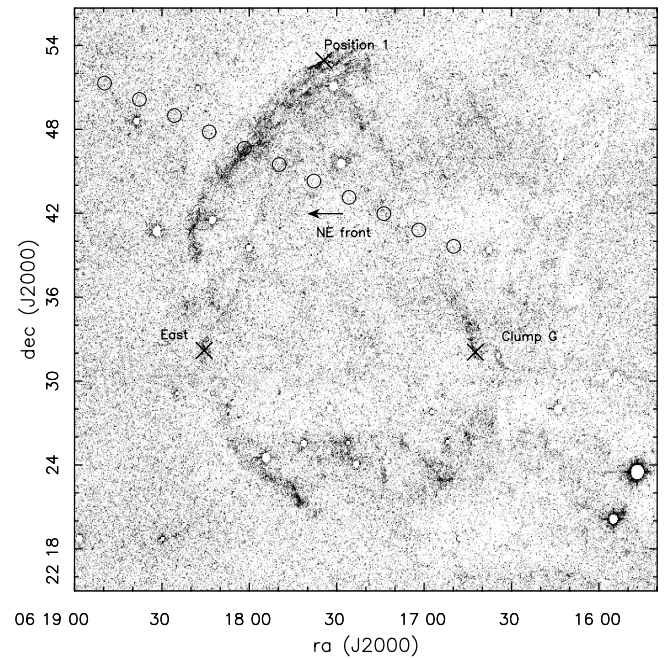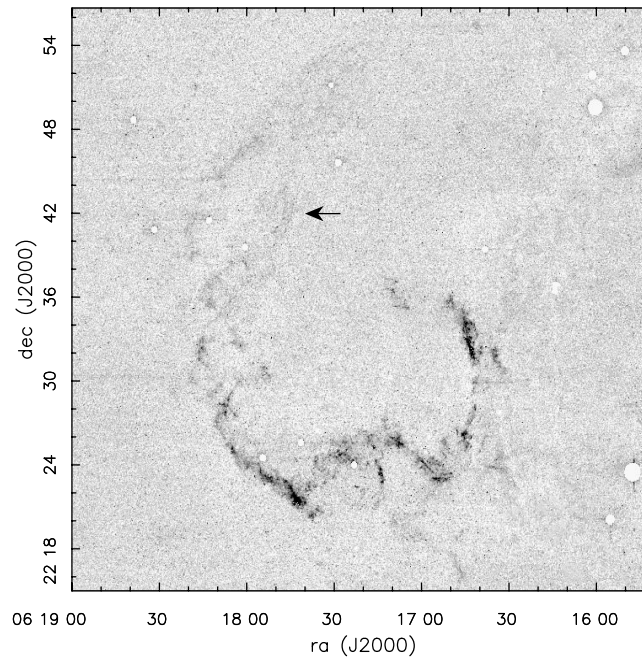
Fɪɢ. 3a

Fɪɢ. 3b

Fɪɢ. 3c

Fɪɢ. 3.—J, H, and K_s images after stars are removed: (a) J-band image, with surface brightness ranging 0.3–6.4 × 10^{-4} ergs s^{-1} cm^{-2} sr^{-1}. (b) H-band image, with brightness ranging from 0.2–4.0 × 10^{-4} ergs s^{-1} cm^{-2} sr^{-1}. (c) K-band image, with brightness ranging from 0.1–12 × 10^{-4} ergs s^{-1} cm^{-2} sr^{-1}. In panel (b), the 11 positions of ISO LWS beam for [O ɪ] observations, "NE front," "position 1," and clump G (south) positions are also marked.

final signal-to-noise was satisfactory ($\gg 10$), clearly detecting the targeted line from seven positions that fall within the remnant. The spectra are shown in Figure 4 and the surface brightnesses are listed in Table 2. The maximum brightness of the [O ɪ] line at position "e" is 4.8 × 10^{-4} ergs s^{-1} cm^{-2} sr^{-1}. The [O ɪ] line is comparable to that of [Si ɪɪ] (34.8 μm; Oliva et al. 1999a), and is twice as bright as [Ne ɪɪ] (12.8 μm) after correction for interstellar extinction. The [O ɪ] line emission peaks at the northeastern shell, where the 2MASS

images showed filamentary structure in J and H. We measured 2MASS H band surface brightnesses from the 11 positions where [O ɪ] brightnesses were measured with the same beam, but large uncertainties of 2MASS surface brightnesses over limited angular scales hinder further comparison of the emitting region structures. The background measurement error was large for relatively weak emission, since the 80″ beam diluted the detected 2MASS emission. The only significant detection is at the peak position "e"
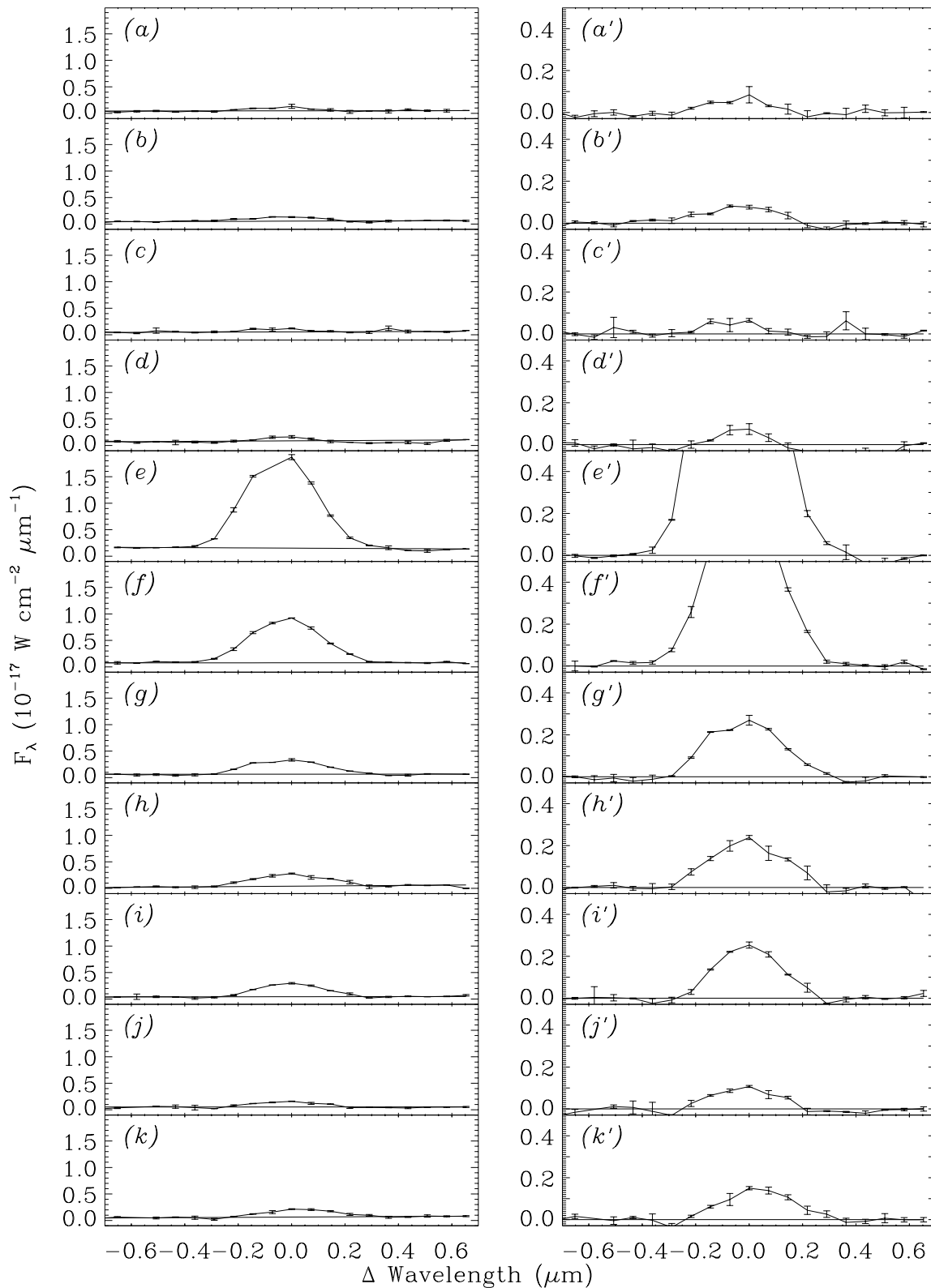
FIG. 4.—*ISO* LWS [O I] spectra of 11 positions. The *y*-axis ranges are adjusted to show weaker lines of the spectra on the right panel. The brightest line at (*e*) has a flux density of 4.8×10^{-4} ergs cm^{-2}s^{-1} sr^{-1}. Spectra from top to bottom are sequential from outside to the interior of the remnant, for the positions marked in Fig. 3*b*. The peak position coincides with northeastern filaments shown in the 2MASS image.

$(2.1 \pm 0.46 \times 10^{-4}$ ergs s^{-1} cm^{-2} sr^{-1}). When we normalize the peak surface brightness between [O I] and H band, the other expected detection in 2MASS band images is from position "*f*," which would be 40% of the peak surface brightness and should have been detected from 2MASS H band accounting for the errors. This suggests possible different shock structures between [O I] and [Fe II]. However, with broadband imaging, this is only a possibility.

TABLE 2

SURFACE BRIGHTNESSES OF [O I] LINES WITH THE POSITIONS USING *ISO*

Position	R.A. (J2000)	Decl. (J2000)	Surface Brightness $(10^{-4} ergs\ s^{-1}\ cm^{-2}\ sr^{-1})$
a	06 18 49.7	+22 51 18.5	0.142 ($\pm$0.018)
b	06 18 37.7	+22 50 08.6	0.202 ($\pm$0.023)
c	06 18 25.7	+22 48 58.7	0.135 ($\pm$0.034)
d	06 18 13.7	+22 47 48.8	0.120 ($\pm$0.054)
e	06 18 01.7	+22 46 38.8	4.814 ($\pm$0.150)
f	06 17 49.7	+22 45 28.7	2.213 ($\pm$0.024)
g	06 17 37.7	+22 44 18.6	0.756 ($\pm$0.044)
h	06 17 25.7	+22 43 08.4	0.653 ($\pm$0.023)
i	06 17 13.8	+22 41 58.2	0.692 ($\pm$0.031)
j	06 17 01.8	+22 40 47.9	0.350 ($\pm$0.023)
k	06 16 49.8	+22 39:37.5	0.403 ($\pm$0.020)

NOTE.—Units of right ascension are hours, minutes, and seconds, and units of declination are degrees, arcminutes, and arcseconds.

2.4. CO *Observation*

We observed a small ($7' \times 12'$) region in the northeastern interior portion of the remnant, centered on R.A. $06^h17^m48''$ and decl. $22°42'00''$ (J2000) using the National Radio Astronomy Observatory 12 meter telescope on Kitt Peak. The position is marked in Figure 3c. The 1 mm receiver was tuned to the CO($2 \to 1$) line, and the spectra were processed with the millimeter autocorrelator for single-point spectra (resolution 0.06 km s^{-1}) and filter banks for mapping (resolution 0.65 km s^{-1}). All spectra were obtained with respect to an absolute reference position located at R.A. $06^h18^m30.0$ and decl. $+22°54'00.0$ (J2000). Maps (see Fig. 8) were obtained using the on-the-fly technique, which yields well-sampled maps (10") with very uniform calibration.

3. LINE EMISSION FROM THE NORTHEASTERN RIM AND COMPARISON WITH SHOCK MODELS

The northeastern shell shows sheetlike filamentary structure similar to the optical emission (Fesen & Kirshner 1980; Mufson et al. 1986). Emission in the J and H bands is equivalently bright for the northeastern shell. The observed $J:H:K_s$ surface brightness ratio is 1:0.7:0.1. This ratio is 1:0.5:0.08 after correcting for extinction, using $A_V = 3.1$ mag (Fesen & Kirshner 1980) and the extinction law given by Rieke & Lebofsky (1985). The 2MASS colors suggest very weak K_s emission in the northeastern rim, $\sim 10\%$ in comparison to the southern part. Previous observations indicate no evidence of H_2 line emission toward the northeastern rim (at the "position 1"; Graham et al. 1987). On the other hand, K_s-band emission for the northeastern rim can be explained by the Brγ line alone.

The possible sources for the northeastern rim emission observed in the J and H bands are H recombination and [Fe II] lines, discounting H_2 emission based on its nondetection by Graham et al. (1987). First, we examined H recombination lines within the 2MASS bands: J, H, K_s bands cover Pβ (1.28 μm), Br10 (1.74 μm), and Brγ (2.17 μm), respectively. The case B ratio of $J:H:K_s$ bands is 1:0.06:0.2, with 3% changes depending on the temperature (2000–20,000 K). We ignore a few other hydrogen lines, because they are orders of magnitude weaker than Br10. The detailed line intensities relative to Hβ depends on the temperatures as shown in Table 3.

Second, we simulated the [Fe II] line intensities within the 2MASS bands. The [Fe II] 1.64 μm line has been shown to be strong in a position on the northeast rim (Graham et al. 1987), with a surface brightness of 1.9×10^{-4} ergs s^{-1} cm^{-2} sr^{-1}. The Brγ line surface brightness is 0.04×10^{-4} ergs s^{-1} cm^{-2} sr^{-1} using the 19".6 aperture, which was much weaker than that of [Fe II] 1.64μm. The H-band

TABLE 3

TEMPERATURE-DEPENDENT HYDROGEN RECOMBINATION AND MOLECULAR H_2 LINE INTENSITIES

Temperature (K)	J	H	K_s	$J:H:K_s$
H Recombination Lines (relative to Hβ)......	(Pβ)	(Br10)	(Brγ)	
T (K)...				
2500	0.21	0.0112	0.0387	1:0.05:0.18
5000	0.187	0.0106	0.0332	1:0.057:0.18
10,000	0.165	0.0092	0.028	1:0.056:0.17
20,000	0.146	0.008	0.0237	1:0.055:0.16
H_2 Line Predictions............................				
T_{ex}				
1000	1.25×10^{-5}	1.31×10^{-5}	0.001073	0.011:0.012:1
2000	4.9×10^{-3}	5.8×10^{-3}	0.034704	0.14:0.167:1
3000	0.033	0.041	0.1165	0.28:0.35:1
4000	0.08117	0.09887	0.2148	0.38:0.46:1

surface brightness at "position 1," 2.4×10^{-4} ergs s^{-1} cm^{-2} sr^{-1}, is slightly brighter than the sum of two H-band lines that have been measured spectroscopically, [Fe II] 1.64 μm (Graham et al. 1987) and Br 10 (see Table 4), which is 1.91×10^{-4} ergs s^{-1} cm^{-2} sr^{-1}. We have calculated line intensities of [Fe II] among 13 levels, with 45 total transitions, by solving the excitation rate equations as a matrix using the atomic data from Nussbaumer & Storey (1988). Our goal is to simulate approximately the lines within the 2MASS bands and examine if the surface brightnesses are comparable to the observed ones. We noticed that the J:H ratio of [Fe II] lines is largely based on the line ratio of [Fe II](1.25 μm)/[Fe II](1.64 μm) = 1.35, set entirely by the atomic data because both lines have the same upper energy level (see Nussbaumer & Storey 1988). Figure 5 illustrates simulated J-, H-, and K_s-band [Fe II] lines, including three lines in J, five lines in H (there were six lines each for the J and H bands, but weak lines are not shown), and no lines in K_s. The simulations show that the J- and H-band emission from [Fe II] largely depends on the 1.25 μm and 1.64 μm lines, respectively, because those two lines are much brighter than others. The J:H ratio changes less than $\sim 30\%$ from 1.35 when including other [Fe II] lines depending on the density and temperature. When we used the [Fe II] line ratio between 17.93 μm and 25.98 μm of 0.5 and between [Fe II] at 1.64 μm and 17.9 μm of 4.2 (Graham et al. 1991; Oliva et al. 1999a), we found a solution with a electron density of 500 cm^{-3} and temperature of 12,000 K. Although these values have a large uncertainty due to different beam size and possibly different filling factors, it should be sufficient to estimate the contributions of [Fe II] lines to J and H bands. Using these physical parameters, the sum of [Fe II] line brightnesses falling in J band, 4.0×10^{-4} ergs s^{-1}, is 1.6 times as large as the sum of [Fe II] line brightnesses in H band, 2.5×10^{-4} ergs s^{-1} cm^{-2} sr^{-1}. Using the predicted estimation of [Fe II] and H recombination lines, the total J, H, and K_s surface brightness are 4.2×10^{-4}, 2.51×10^{-4}, and 0.04×10^{-4} ergs s^{-1} cm^{-2} sr^{-1}, respectively. These

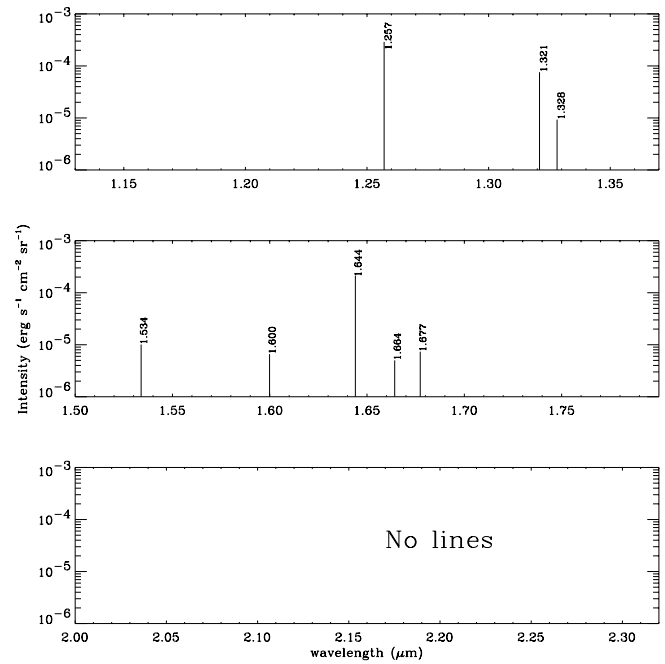Fig. 5.—Estimate of the contribution of [Fe II] line intensity to J-, H-, and K_s-band emission.

results are consistent with the observed surface brightnesses (see Table 1) considering various uncertainties such as the beam size and error of the each measurement. We conclude that along the northeastern rim the J-band emission is composed of [Fe II] ($\sim 90\%$) and Pβ ($\sim 10\%$), the H band is [Fe II] ($\sim 99\%$) and Br10 ($\sim 1\%$), and the K band is Brγ.

We have listed the surface brightnesses of [Fe II] lines, [O I] and other detected infrared and optical lines from "position 1" in the northeastern rim (Oliva et al. 1999a; Fesen & Kirshner 1980) in Table 4. We have compared these surface brightnesses with various shock models. A fast

TABLE 4

IR LINES AND THEIR FLUXES IN THE NORTHEASTERN RIM

Line	λ (μm)	Unreddened Flux (10^{-13} ergs s^{-1} cm^{-2})	Beam (arcsec)	Surface Brightness (10^{-4} ergs s^{-1} cm^{-2} sr^{-1})	Reference
Hβ	4861 Å	20.8	2.8 × 40	8	1
[Fe II]...................	1.257	...	model	2.6	this work
Pβ	1.28	...	model	0.2	this work
[Fe II] in J band	6 lines	...	model	4.0	this work
Total J band	...	...	...	4.2, 4.49 ± 0.63[b]	this work
[Fe II]...................	1.644	13.3	19.6	1.9	2
[Fe II] in H band......	6 lines	...	model	2.5	this work
Br10....................	1.74	...	model	0.012	this work
Total H band	...	...	...	2.51, 2.4 ± 0.6[b]	this work
Brγ	2.165	0.3	19.6	0.04	2
[Ne II]	12.8	18	14 × 27	2.02 ± 0.34	3
[Ne III]	15.56	10	14 × 27	1.12 ± 0.23	3
[Fe II]...................	17.93	4	14 × 27	0.45	3
[S III]	18.71	4	14 × 27	0.45	3
[O O IV]	25.88	3	14 × 27	0.34	3
[Fe II]...................	25.98	8	14 × 27	0.89 ± 0.11	3
[Si II]	34.8	52	20 × 33	3.35 ± 0.45	3
[O I]...................	63	570	80	4.80	this work

[a] A single number indicates the diameter of a circular beam.
[b] The two numbers are model and observed surface brightnesses, respectively.
REFERENCES.—(1) Fesen & Kirshner 1980; (2) Graham et al. 1987; (3) Oliva et al. 1999a.

J-shock model in Hollenbach & McKee (1989, hereafter HM) with a density of 10^3 cm^{-3} and a shock velocity of 80–100 km s^{-1} is consistent with most of the detected lines such as [Ne II] (12.8 μm), [Fe II] (17.93μm and 25.98 μm), and [O I] (63 μm). The comparison with the HM model shows that a lower shock velocity with a density of 10^3 cm^{-3} predicts much weaker [Ne II] than observed, and all observed lines are too weak for a higher density of 10^4–10^6 cm^{-3}. However, there are still two important differences between the data and the most consistent shock model with a density of 10^3 cm^{-3} and a shock velocity of 80–100 km s^{-1} of HM. First, multi-ionized ion species like [Ne III], [S III] and [O IV] are not included in the model, thus it is not clear whether a fast J-shock model with $V_s = 80$–100 km s^{-1} can explain the highly ionized species or a higher shock velocity is required. Second, the observed [Si II] (34.8 μm) line is at least a factor of 5 stronger than that in the HM model. We discuss below if these differences infer other types of shocks, V_s, and/or n_o.

We compared other shock models (Hartigan, Raymond, & Hartman 1987; McKee, Chernoff, & Hollenbach 1984) using shock diagnostic plots for different shock velocities and/or densities. Since multi-ionized species are expected from high velocity shocks, we have checked if the observed [Ne III] requires a higher shock velocity, or if it can be produced by $V_s \sim 100$ km s^{-1}. The ratio of [Ne III] to [Ne II] is shown as a function of shock velocity in Figure 6a using the shock models of Hartigan et al. (1987). The observed ratio of 0.55 ± 0.15 implies two possible shock velocities of $V_s = 100 \pm 20$ km s^{-1} and 250 ± 30 km s^{-1}. While the overall tendency is that the ratio increases as the shock velocity increases, the ratio also shows a bump around 100 km s^{-1} which is due to the shape of the cooling function. Figure 6a shows that the observed ratio of [Ne III] and [Ne II] is consistent with the J-shock models of $V_s \sim$ 80–120 km s^{-1}. The absolute surface brightnesses of [Ne II], [Fe II] (25.98 μm), and [Si II] can be used to measure the shock velocity: they are too weak for a high-velocity shock of ~ 250 km s^{-1} as shown in Figure 6b. The shock velocity inferred from the brightnesses of three lines are marked with a thick solid line in Figure 6b, where the allowed shock velocity, using the overlapped shock velocity from the three lines, ranges between 80–120 km s^{-1}. The surface brightness in Table 4 assumes that emission is filled within the beam. So if the filling factor is in fact smaller, the surface brightness is conversely larger than the values given. The slightly lower shock velocities are inferred even if [Ne II] and [Fe II] (25.98 μm) have a factor of 5–7 smaller filling factor. The brightness of [Si II] shows that if the surface brightness (due to smaller filling factor) is greater than 1.5 times of the current value in Figure 6b, no shock velocity solution is found. In summary, both the observed line brightnesses of [Ne II], [Si II] and [Fe II] and the ratio of [Ne III]/[Ne II] are consistent with V_s of ~ 100 km s^{-1}, and the line brightnesses are more than a factor of 4–5 lower than predictions for higher (>150 km s^{-1}) velocity shocks.

We have compared the detected infrared line intensities with those for the remnant RCW 103, which is undergoing a high velocity shock, $V_s \sim 250$ km s^{-1} (Oliva et al. 1999b). In contrast, many lines from IC 443 are much weaker (at least an order of magnitude) than those of RCW 103, in particular [Fe II]. The intercloud shock velocity for IC 443 and RCW 103 is 800 km s^{-1} (Petre et al. 1988) and 12,000 km s^{-1} (Nugent et al. 1984), respectively, which is primarily
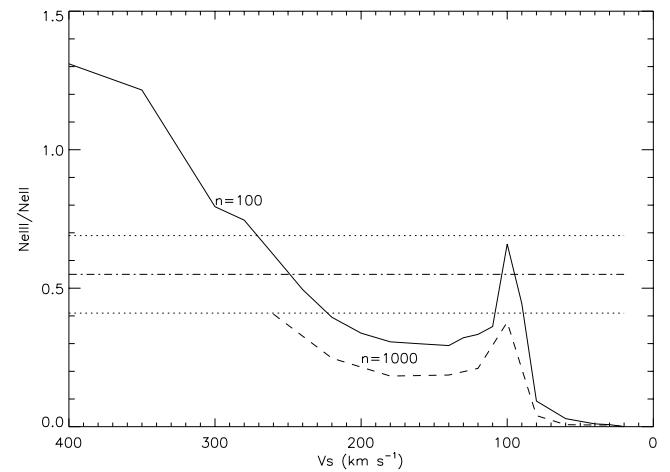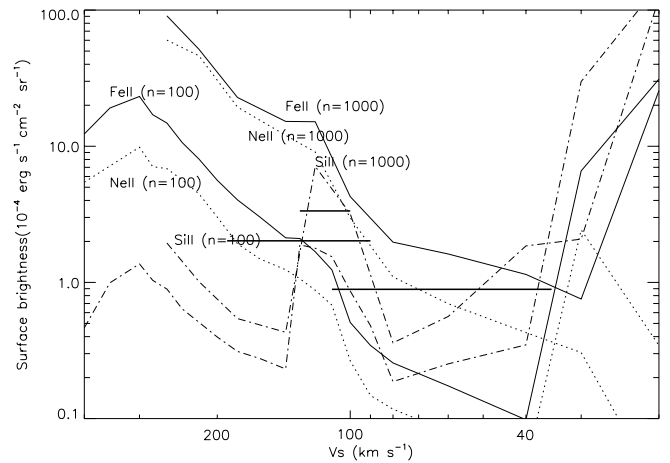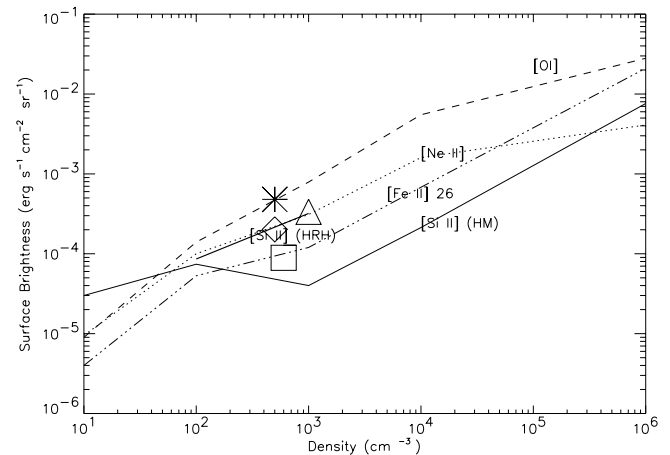

FIG. 6a

FIG. 6b

FIG. 6c

FIG. 6.—(a) The [Ne III]/[Ne II] ratio as a function of shock velocity. The upper and lower limits from the errors are marked as dotted lines. (b) Constraint on a shock velocity using the line brightnesses of [Ne II], [Fe II], and [Si II] lines. The allowed shock velocity ranges are marked with thick lines for each line brightness. (c) Shock model predictions of the line brightnesses as a function of density from McKee et al. (1984) using a shock velocity of 100 km s^{-1}. The observed values are marked for [O I], [Ne II], [Fe II], and [Si II] by an asterisk, diamond, square, and triangle, respectively.

related to the age difference between remnants: IC 443 age is 5000–10,000 yr (Petre et al. 1988) and RCW 103 is 1000 yr (Nugent et al. 1984). The shock velocity ratio between cloud medium and intercloud medium is inversely proportional to the square root of the density ratio. The lower shock velocity of 100 km s^{-3} in IC 443 compared with that of RCW 103 is probably related to the remnant age, since the preshock density of RCW 103 (10^3 cm^{-3}) is comparable to that of northeastern rim of IC 443. On the other hand, a high-velocity shock greater than 150 km s^{-1} is not stable; hence, comparison with the steady shock model may not be meaningful for this scenario (see review in Draine & McKee 1993; Innes, Giddings, & Falle 1987).

We explored the possible preshock density range of the preshock medium at the northeastern rim. Figure 6c shows a set of predicted line brightnesses as a function of density based on McKee et al. (1984), where density ranges from $10–10^6$ cm^{-3}, covering a larger density range than those in Hollenbach & McKee (1989). The observed surface brightness for these lines at a density of 300–1000 cm^{-3} agrees with the models in McKee et al. (1984) and Hollenbach & McKee (1989), except for the [Si II] line, as shown in Figure 6c. Note however, the observed surface brightness of [Si II] is consistent with those in Hartigan et al. (1987) model, as discussed before. The difference is due to metal abundance since the Hartigan models used higher abundances of Si (3.23×10^{-5}) while the HM model used a smaller value of 3.6×10^{-6}. While the Hartigan model did not use dusty radiative transfer and assumed complete grain destruction, the HM model includes dusty radiative transfer and accounts for grain destruction. Therefore, it suggests that either the intrinsic abundance of Si is higher than predicted or more efficient grain destruction occurs. The grain destruction depends on a wide array of physical parameters (detailed in Jones, Tielens, & Hollenbach 1996), requiring further theoretical exploration. Finally, a low preshock density of ~ 10 cm^{-3} for the near-infrared–emitting region can be ruled out based on the observed values for the northeastern rim of IC 443 as shown in Figure 6c; the observed brightnesses of [O I] and [Fe II] are too strong for a density of 1–10 cm^{-3}. This conclusion is even true if the filling factor of the emission in our beam is small. The Cygnus Loop is consistent with the shock model prediction of a density of 1–10 cm^{-3} and a shock velocity of 100 km s^{-1} (McKee et al. 1987). The model predicted [O I] and [Si II] brightnesses for a density of 10 cm^{-3} and a shock velocity of 30 km s^{-1} are 2×10^{-6} and 6×10^{-7} ergs s^{-1} cm^{-2} sr^{-1}, respectively, which are too weak for the observed brightnesses of IC 443. A low-density (< 10 cm^{-3}) and a low shock velocity model is not consistent with that of IC 443. We note there is a limitation in comparison of the observed brightnesses with shock models, because the shock structures are not resolved with available data. The observed values are measured with different beam sizes, and it is also possible that the shock is tilted and/or multiple-shocks are present within the beam. Higher angular resolution imaging of the infrared lines are needed for further study.

4. SHOCKED MOLECULAR LINES OF THE SOUTHERN RIDGE AND COMPARISON WITH SHOCK MODELS

In contrast to the northeastern rim, the southern ridge is dominated by K_s-band emission, exhibiting a knotty structure (Fig. 3c). In this direction, the extinction is 3.3 mag in

A_V (Burton et al. 1988), and the $J:H:K_s$ ratio of 0.2–0.33:0.36:1 becomes 0.35–0.5:0.4:1 after correcting for this extinction. The shocked H_2 line emission, especially H_2 1-0 S(1) (2.12 μm) in the K_s band, is well known from the southern ridge (Burton et al. 1988), and it is produced by an interaction with dense molecular clouds. The measured K_s-band surface brightness is $2.44 \pm 0.18 \times 10^{-4}$ ergs s^{-1} cm^{-2} sr^{-1} (Table 1), which includes a dozen lines as shown in Figure 7b, among which the brightest lines are 1-0 S(1) (2.12 μm), 1-0 S(2) (2.03 μm), and 1-0 S(0) (2.22 μm). This brightness is approximately equal to a sum of the two detected lines [1-0 S(1) at 2.122 μm, and 1-0 S(0) at 2.223 μm] by Burton et al. (1988) toward clump C. The predicted
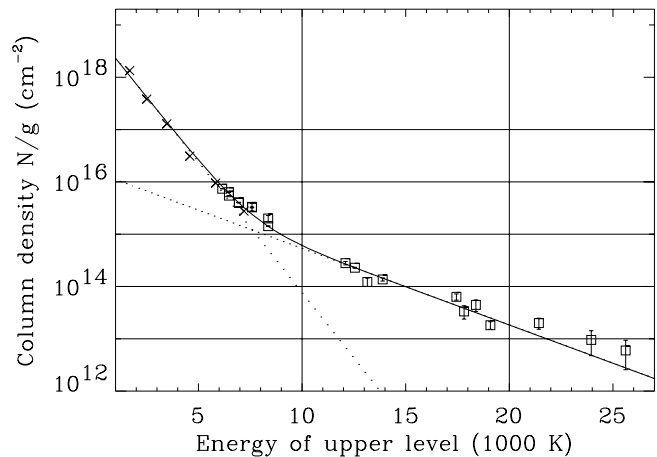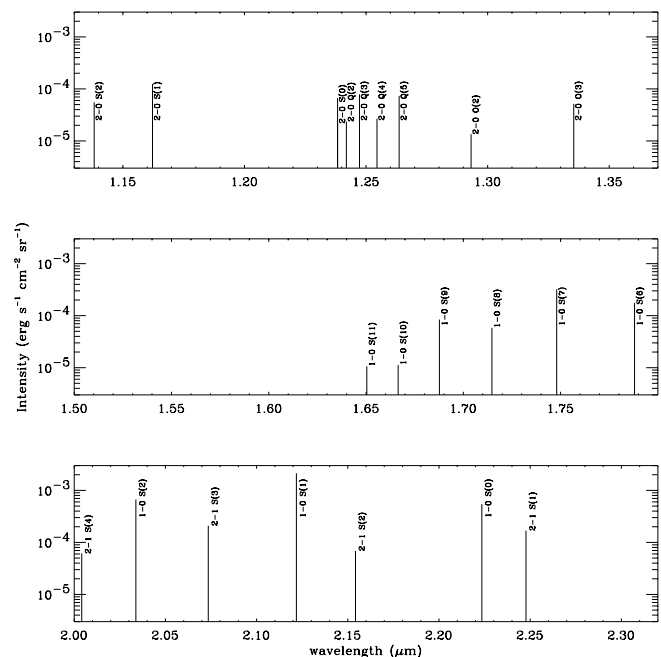

FIG. 7a

FIG. 7b

FIG. 7.—(a) Population level diagram as a function of upper state energy for H_2 lines. Near-infrared (Richter et al. 1995) and mid-infrared ISOCAM data (Cesarsky et al. 1999) are shown with squares and crosses, respectively, from which a two temperature model (solid line) of excitation are derived. The two dotted lines are $T_{ex(1)} = 870$ K and $T_{ex(2)} = 2970$ K. (b) Estimation of contributed H_2 line intensity to J-, H-, and K_s-band emission.

H recombination and H_2 line brightness and the $J:H:K_s$ ratio using excitation temperatures ranging from 1000–4000 K, are listed in Table 3. Note that the H_2 ratios are very sensitive to the excitation temperature.

Can the J- and H-band emission come from hydrogen recombination lines? Burton et al. (1988) has searched spectroscopically for Brγ lines, yielding a nondetection with the upper limit of 0.042×10^{-4} ergs s^{-1} cm^{-2} sr^{-1} (from 3×10^{-14} ergs s^{-1} cm^{-2} for 19″.6 aperture diameter). Using the upper limit of the extinction corrected brightness of 6×10^{-6} ergs s^{-1} cm^{-2} sr^{-1}, the Pβ (for J band) and Br10 (for H band) brightnesses should be less than 0.13×10^{-4}, and 0.01×10^{-4} ergs s^{-1} cm^{-2} sr^{-1}, respectively. It seems unlikely that the H-band flux is coming from the hydrogen recombination line of Br10, although the flux of Pβ might contribute to some portion of the J-band flux. Using an upper limit for the Brγ line, the Pβ contribution could be as large as 7% of J-band surface brightness.

We have estimated H_2 intensities within the 2MASS bands by deriving excitation temperatures from the many near- and mid-infrared spectral lines spanning the energy levels that contribute the lines in the 2MASS bands. The ISOCAM data from Cesarsky et al. (1999) for 5–14 μm were fitted to a two-temperature model with the excitation temperatures $T_1 = 657$ K and $T_2 = 1288$ K and the respective column density of 2.2×10^{20}, and 0.22×10^{20} cm^{-2}. The ISOCAM data (Cesarsky et al. 1999) and the ground-based near-infrared data by Richter et al. (1995) are shown in Figure 7a. While the ISOCAM lines have upper energy levels of less than 7000 K, the ground-based data appear at 5000–26,000 K. By fixing two excitation temperature components obtained from ISOCAM data, a third temperature component ($T > 1288$ K) is needed to fit both sets of data. Unfortunately, the ISOCAM data alone were not adequate to constrain the high-temperature component. Therefore, we have developed a new two excitation temperature model to fit both near-infrared and mid-infrared data. The optimum values for the two temperatures and the corresponding column densities are $T_{\mathrm{ex}(1)} \sim 870$ K and $N_1 \sim 1.3 \times 10^{21}$ cm^{-2}, and $T_{\mathrm{ex}(2)} \sim 2970$ K and $N_2 \sim 4.0 \times 10^{18}$ cm^{-2}, respectively. With this model, the estimated J-:H-band ratio is 0.8 and the H-:K_s- band ratio is 0.2. These ratios are lower than observed values of 1.1 and 0.4, respectively. We calculated the brightness of all lines that fall in the 2MASS bands. The lines have upper energy levels of 11,000–14,000 K for J band, 10,000–19,000 K for H band, and 12,000–15,000 K and 18,000–20,000 K for K_s band. The contributed H_2 lines to 2MASS bands are shown in Figure 7b.

There are two possibilities to explain the excess J- and H-band emission, relative to the H_2 model. First, the excess J- and H-band emission might still be from H_2 lines only, considering that the accurate prediction requires a nonsteady C-shock model as shown in Cesarsky et al. (1999). The fact that the image morphology of J and H bands in the south, in particular at the clump G position (see Figs. 3a and 3c), is very similar to that of K_s band and different from that of optical emission, supports that the J- and H-band emission is from H_2 lines. It is possible that the nonsteady C-shock model could explain the observed $J:H:K_s$ ratio using only H_2 lines. When we increase the second temperature and decrease the first temperature, we can obtain a reasonable fit (except for the upper energy levels of 6000–8000 K), for which the $H:K_s$ ratio is close to 0.4. However,

the $J:H$ ratio greater than 1 cannot easily be explained using H_2 lines only.

The second possibility is that the remaining J- and H-band emission is from [Fe II] lines, and some portion of J-band emission is from Pβ. We also measured another southern position (R.A. 06^{h}17^{m}7^s.6 and decl. $+22°25'35''$ [epoch J2000]; "south ridge position") where an *ISO* SWS spectrum is available. The 2MASS $J:H:K_s$ ratio for this position is similar to that of the position "south (clump G)". *ISO* archival data show a clear detection of [Si II] (34.8 μm), but the presence of [Fe II] (26 μm) is uncertain. The upper limit of [Fe II] (26 μm) is 3×10^{-5} ergs s^{-1} cm^{-2} sr^{-1}. A region with no [Ar II], [Ar III], and [Ne II] (like in ISOCAM data) can still emit [Si II] and [Fe II] because the latter has lower ionization potentials. The brightness ratio between [Fe II] 26 μm and 1.25 μm is very sensitive to temperature; it can change between 0.2–1000 with the higher temperature giving a lower ratio. A very hot, low-ionization gas could make enough emission to contribute to the J and H bands at the levels observed; however, we lack sufficient spectroscopic data to resolve the origin of the excess emission in the southern part of IC 443.

The far-infrared line [O I] 63 μm was first detected in IC 443 by Burton et al. (1990). The authors suggested the presence of two shocks to explain the [O I] and the shorter-wavelength H_2 lines, either a C-shock with a dissociative J-shock with suppressed oxygen chemistry, or alternatively, two-shock models (a high and low shock velocity). CO observations of Wang & Scoville (1992) suggest the presence of a J-shock from the broadline CO gas. This implies that a mixture of J- and C-shocks are present in a small-scale clump. However, recent ISOCAM observations toward southern region, clump G, shows that no ion lines were detected, while only molecular hydrogen lines have been detected (Cesarsky et al. 1999). A fast J-shock would have emitted rich lines from all abundant elements. The ISOCAM observational result is rather surprising and remarkable given that a J-shock component must be present (Burton et al. 1990). In comparison, other molecular interacting supernova remnants, 3C 391, W44, and W28 showed many atomic lines, including strong [Fe II] and [Si II], and molecular hydrogen lines with *ISO* (Reach & Rho 2000). Cesarsky et al. (1999) showed that the detected pure rotation lines of molecular hydrogen are consistent with a time-dependent C-shock model with a shock velocity of 30 km s^{-1} and a preshock density of 10^4 cm^{-3}. Likewise, a C-shock with a density of 10^4 cm^{-3} and a shock velocity of 30 km s^{-1} accounts for a large portion of the 2MASS band emission with H_2 lines. However, it is still unclear if the broad CO line is due to a slow J-shock as suggested by Wang & Scoville (1994) or due to a C-shock. Comparison of high-resolution spectra of the two lines would be an important diagnostic for understanding the type of shock for [O I] and broad CO lines.

5. EXTENT OF THE SUPERNOVA MOLECULAR CLOUD INTERACTION

The shocked H_2 line map is well observed from the southern sinuous ridge (Burton et al. 1988; Richter 1995). The shocked CO gas with broad lines is also intensively observed from the same, southern region (Dickman 1992; van Dishoeck et al. 1993). The large field of view of the 2MASS image shows that the H_2 emission extends to the east and the inner side of the northeastern rim of the
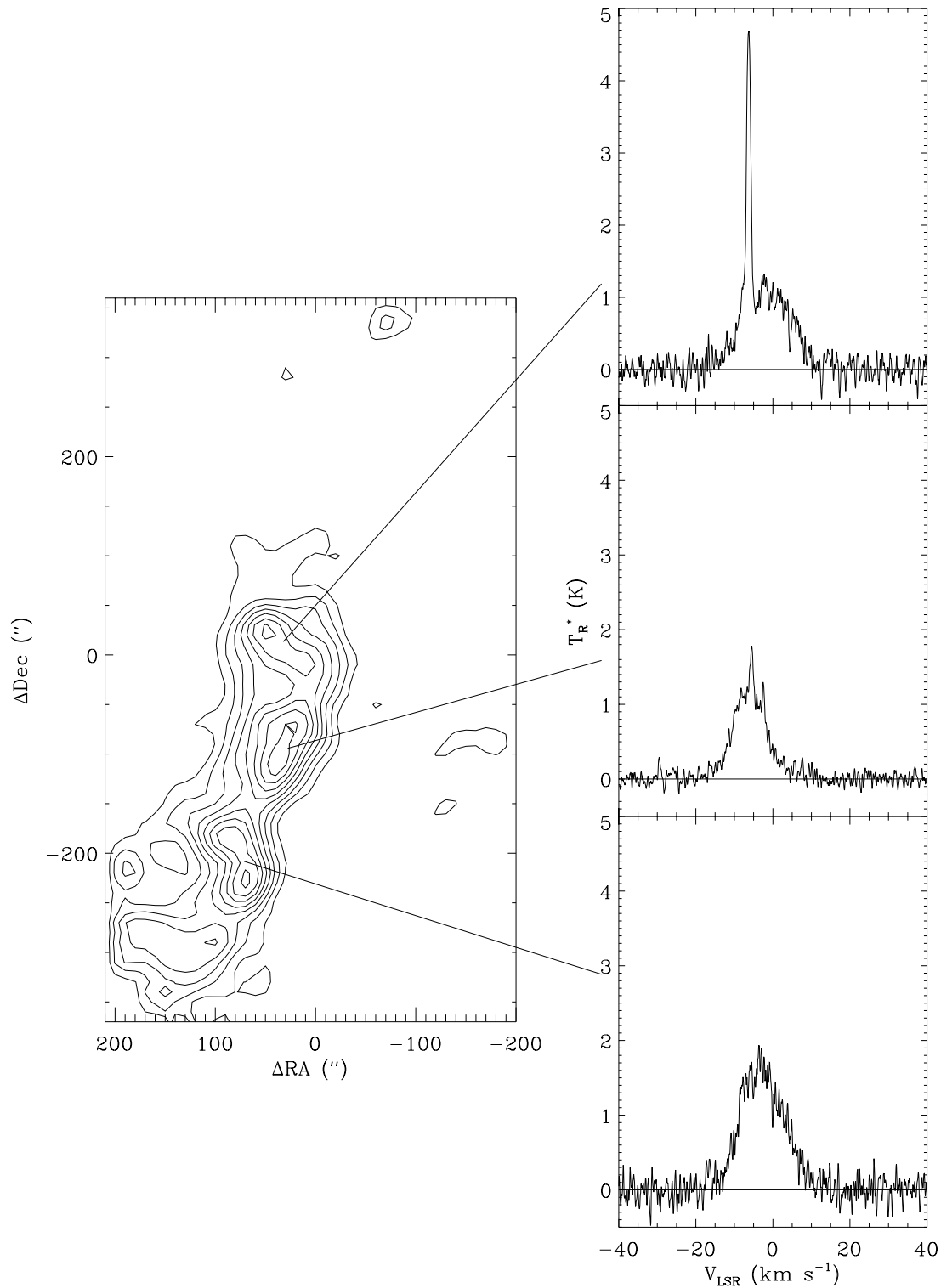
Fig. 8.—CO($2 \rightarrow 1$) map contours. The map center is at R.A. $06^{h}17^{m}48^{s}$ and decl. $+22°42'$ $00.0''$ (J2000), where an arrow is marked in Fig. 3c. On the right-hand side are three CO($2 \rightarrow 1$) spectra along the filament, showing the separation into broad and narrow components.

remnant as seen in Figure 1. The H_2 emission in the inner part of the northeastern rim is most clearly seen in the mosaiced color image (red in Fig. 1; the area is marked with an arrow in Fig. 3c). We measured the $J:H:K_s$ surface brightnesses at the position ("NE front" in Table 1: R.A. $06^{h}17^{m}48^{s}$ and decl. $+22°41'58''$) defined by an ellipse with a radius of $60'' \times 110''$ and a position angle of 351°. The K_s emission is much stronger than J or H, with the $J:H:K_s$

ratio of 0.3:0.4:1 using $Av = 3.1$ mag. This ratio is comparable to that of the southern sinuous ridge, suggesting the H_2 lines are primary contributors. The molecular cloud, as traced with CO emission, has been shown to stretch across the entire remnant, which includes extending to the northeastern part (Cornett et al. 1977). The K_s-band emission from the inner part of the northeastern rim suggests that this region is also interacting with the molecular clouds.

TABLE 5

COMPARISON OF PHYSICAL PROPERTIES OF INFRARED-EMITTING REGIONS BETWEEN
THE NORTHEASTERN RIM AND THE SOUTH

Parameters	Northeastern Rim	South Sinuous Ridge
Dominant IR lines......	[Fe II], [Ne II],[Si II], [O I]	H_2, [O I]
Type of shock	fast J-shock	C-shock
Density (n_o)	$10 < n_o < 10^3$ cm^{-3}	$\sim 10^4$ cm^{-3}
Shock velocity (V_s)	80–110 km s^{-1}	40 km s^{-1}

The interaction is likely the front side of IC 443, since the molecular clouds are in the front of the remnant (Cornett et al. 1977; Asaoka & Aschenbach 1994).

In order to determine whether the widely distributed K_s-band emission in the northern interior of the remnant is related to shocked molecular gas, we compare to CO observations. A CO($1 \rightarrow 0$) survey of IC 443 revealed numerous shocked clumps, of which the smallest was labeled clump H (Dickman et al. 1992). This clump is separated from the southern sinuous ridge, and it is weaker than the others. The 2MASS image in this region reveals many clumps embedded in filamentary emission. Our follow-up observations with the NRAO 12 m have high enough angular resolution and sensitivity to allow a detailed comparison. Figure 8 shows the CO map where K_s emission is detected (where an arrow is marked in Fig. 3c) with three spectra. The fact that broad CO lines are detected where K_s-band emission appears, suggests that K_s emission is due to shocked H_2 lines. The CO emission consists of a filament with a few distinct clumps. The panels in Figure 8 show spectra at three positions along the filament. The spectra consist of a broad component, with a FWHM of 14 km s^{-1} and a narrow emission component with a FWHM of 1.2 km s^{-1}. The broad component of the CO emission is due to shocked gas; it does not break into narrow components when viewed at high spatial or spectral resolution. The width of the broad component is comparable to other places in the southern ridge, and the velocity center follows the systematic variation of the rest of the ridge (Dickman et al. 1992). Our CO($2 \rightarrow 1$) observations along with K_s-band image therefore for the first time show that clump H is part of the supernova-molecular cloud interaction. The good correspondence between the CO map and the K_s-band map in this region demonstrates that the physical properties of the shocked gas are probably similar to those in the southern sinuous ridge. By inference, then, it is almost certain that the extended K_s-band emission at this location is due to H_2 line emission.

The physical and shock properties between the northeastern rim and southern ridge are compared in Table 5. Although the shock parameters are primarily measured from "position 1" and "clump G" position, they are likely representing the northeastern rim and southern sinuous ridge, respectively, since 2MASS images and surface brightnesses show similar J:H:K_s ratios. The strong H_2 lines are detected for most of the southern ridge while no ionic lines are detected so far from "clump G" position. However, the J:H:K_s ratio changes gradually from the south, to the east, and to the northeastern rim. The flux of the eastern position is measured as shown in Table 1. The targeted region of the "east" position is defined by an ellipse with a radius of $36'' \times 71''$ and an angle of $352°$ at the position of R.A. $6^h18^m15^s.5$, and decl. $22° 32'11''.4$ (J2000). The extinction $A_V = 3.17$ mag, an intermediate value between the north-

eastern rim and south, is used for the "east" position. The J:H:K_s ratios of the eastern positions correspond to those between the northeast and southern ridge. The K_s:J ratio of 0.7 is much stronger than that seen in the northeastern rim. This suggests that both [Fe II] and H_2 emission can be present from the eastern region. One eastern region shows similar J:H:K_s ratio at this position and Graham et al. (1987) detected both [Fe II] and H_2 lines. Therefore, the emission lines of both ion and H_2 must be combined in the eastern region, and the regions of J- and C-shocks could be associated. The C-shock may be developed in a dense clump while J-shock is developed in a lower preshock density cloud surrounding the clump where the molecules are dissociated by a strong shock. The eastern region shows combination of ionic and H_2 lines as observed in other remnants including 3C 391, W44, and W28, within an ISO LWS beam (Reach & Rho 2000). The clear distinction between the northeastern and southern sinuous ridge of IC 443 as inferred from 2MASS color is striking, delineating the J- and C-shocks.

6. NEAR-INFRARED LUMINOSITY OF IC 443

We estimated the total luminosity of J, H, and K_s bands, by summing the emission in the starlight-subtracted image. The total flux is 11.6, 6.4 and 9.8×10^{-10} ergs s^{-1} cm^{-2} for the J, H, and K_s bands, respectively, with $\sim 20\%$ uncertainty due to the background subtraction and residuals from removed bright stars. The extinction corrected luminosity using a distance to IC 443 of 1.5 kpc is 6.5, 2.6, and 3.4×10^{35} ergs s^{-1}, respectively. The total near-infrared luminosity is 1.3×10^{36} ergs s^{-1}. The separate H_2, [Fe II] and hydrogen recombination line luminosities within 2MASS bands are estimated based on the contributed portion of their emission to J, H, and K_s bands, respectively, which was described in sections 3 and 4. We have first estimated H_2 luminosity for the J, H, and K_s bands, which is 1.3, 1.4, and 3.4×10^{35} ergs s^{-1}, respectively, based on the H:K_s of 0.4 and J:H of 0.8 and assuming that most of K_s band is from H_2 lines. The total H_2 luminosity of J, H and K_s bands is 6.1×10^{35} ergs s^{-1}. The total [Fe II] luminosity is 5.9×10^{35} ergs s^{-1} based on 90% of the J band and 99% of H band flux after excluding J and H band contribution from H_2 emission. The hydrogen recombination line luminosity is 10% of J-band and 1% of H-band flux after excluding the J and H band contribution from H_2 emission. The total hydrogen recombination line luminosity is 0.53×10^{35} ergs s^{-1}. These luminosities have large uncertainties because fixed contribution ratios of H II, H_2 and [Fe II] (§§ 4 and 4) are used from the northeastern rim and the southern ridge, respectively, and it did not account for the gradual changes in the flux ratios to the east and to northeast. In addition, there is still some uncertainty in understanding the J- and H- band emission in the south. In summary, the total luminosities of H_2, [Fe II] and hydrogen

recombination lines in the near-infrared bands are 6.1×10^{35}, 5.9×10^{35} and 0.53×10^{35} ergs s^{-1}, respectively.

7. CONCLUSIONS

1. Near-infrared emission from IC 443 was detected in J, H, and K_s in the Two Micron All Sky Survey (2MASS) Atlas Images, showing a shell-like morphology. The northeastern shell is delineated into a sheetlike filamentary structure with the J- and H-band emission dominating the near-infrared, while southern sinuous ridge emission shows knotty structure with K_s-band emission dominant. These are the first J, H, K_s near-infrared images that cover the entire remnant. The color and structure show contrast between the northeastern and southern parts as shown in Figure 1.

2. The northeastern shell exhibits equivalent brightness between the J and H bands, with a $J:H:K_s$ surface brightness ratio of 1:0.5:0.08 after extinction correction. The K_s-band emission is likely from Brγ recombination, since no H_2 lines have been previously detected. We estimated possible [Fe II] lines and their line strengths with 2MASS bands by solving the excitation rate equations and using the 2MASS fluxes and previously detected [Fe II] lines. The primary line ratio of 1.24 μm/1.64 μm ~ 1.35 set by atomic physics was mainly important to determine the $J:H$ ratio, and the total [Fe II] line brightness falling in J band is 1.6 times as large as [Fe II] line brightness in the H band estimated from the observed line ratios. Thus we conclude that the H-band emission is composed of [Fe II] ($>99\%$) and Br10 ($<1\%$), and the J-band emission of [Fe II] ($\sim 90\%$) and Pβ ($\sim 10\%$).

3. We obtained positive detections of [O I] (63 μm) for 11 positions in the northeast using ISO LWS observations. The [O I] line emission peaks at the northeastern shell, where the 2MASS images showed filamentary structure in J and H. The surface brightness of the brightest [O I] line corresponds to a surface brightness of 4.8×10^{-4} ergs s^{-1} cm^{-2} sr^{-1}, which is comparable to that of [Si II].

4. In contrast to the northeastern rim, the southern ridge is dominated by K_s-band emission, with the extinction-corrected $J:H:K_s$ ratio of 0.35–0.5:0.4:1. The shock-tracing H_2 1-0 S(1) 2.12 μm line is clearly mapped for the southern sinuous ridge. We have developed a new two excitation temperature model to fit both near-infrared ground-based and mid-infrared ISOCAM data. The derived value for the J-:H-band ratio is 0.8, and for the H-:K_s-band ratio is 0.2, which are smaller than those observed. Therefore, most of K_s band and approximately half of the J- and H-band emission can be explained only with the H_2 lines. Some contribution of Pβ and other ionic lines to the J and H bands is possible.

5. Comparison of the dominant shocks and the physical parameters between the northeastern rim and the southern sinuous ridge is summarized in Table 5. The infrared emission from the northeastern rim is mostly from ionized atomic lines and some neutral oxygen line [O I], with no evidence of molecular hydrogen lines. A fast J-shock model with a shock velocity of 80–110 km^{-1} and a density of $10 < n_o \lesssim 1000$ cm^{-3} is consistent with the observed lines from the northeastern rim. The infrared emission from the southern ridge comes from molecular H_2 and [O I]. The dominant shock is a slow C-shock with a $v_s = 30$ km s^{-1} and $n_o = 10^4$ cm^{-3}.

REFERENCES

Arendt, R. G. 1989, ApJS, 70, 181
Asaoka, I., & Aschenbach, B. 1994, A&A, 284, 573
Braun, R., & Strom, R. G. 1986, A&A, 164, 193
Burton, M. G., Geballe, T. R, Brand, P. W., & Webster, A. S. 1988, MNRAS, 231, 617
Burton, Michael G., Hollenbach, D. J., Haas, M. R., Erickson, E. F. 1990, ApJ, 355, 197
Cesarsky, D., Cox, P., Pineau des Forets, G. P., van Dishoeck, E. F., Boulanger, F., & Wright, C. M. 1999, A&A, 348, 945
Cornett, R. H., Chin, G., & Knapp, G. R. 1977, ApJ, 54, 889
Dickman, R. L., Snell, R. L., Ziurys, L. M., & Huang, Y.-L. 1992, ApJ, 400, 203
Draine, B. T., & McKee, C. F. 1993, ARA&A, 31, 373
Dwek, E., & Arendt, R. G. 1992, ARA&A, 30, 11
Fesen, R. A., & Kirshner, R. P. 1980, ApJ, 242, 1023
Giovanelli, R., & Haynes, M. P. 1979, ApJ, 230, 540
Graham, J. R., Wright, G. S., & Longmore, A. J. 1987, ApJ, 313, 847
Hartigan, P., Raymond, J., & Hartmann, L. 1987, ApJ, 316, 323
Hollenbach, D., & McKee, C. F. 1989, ApJ, 342, 306 (HM89)
Innes, D. E., Giddings, J. R., & Falle, S. A. E. G. 1987, MNRAS, 226, 671
Jones, A. P., Tielens, A. G. G. M., & Hollenbach, D. J. 1996, ApJ, 469, 740
McKee, C. F. 1987, Spectroscopy of Astrophysical Plasmas, ed. A. Dalgarno & D. Layzer (Cambridge: Cambridge Univ. Press)

McKee, C. F., Chernoff, D. F., & Hollenbach, D. J. 1984, Galactic and Extragalactic Infrared Spectroscopy, ed. M. F. Kessler & J. P. Phillips
Mufson, S. L., et al. 1986, AJ, 92, 1349
Nugent, J. J., Pravdo, S. H., Garmire, G. P. Becker, R. H. Tuohy, I. R., & Winkler, P. F. 1984, ApJ, 284, 612
Nussbaumer, H., & Storey, P. J. 1988, A&A, 193, 327
Oliva, E., Lutz, D., Drapatz, S., & Moorwood, A. F. M. 1999a, A&A, 341, 75
Oliva, E., Moorwood, A. F. M., Drapatz, S., Lutz, D., & Sturm, E. 1999b, A&A, 343, 943
Petre, R., Szymkiwiak, A. E., Seward, F. D., & Willingale, R. 1988, ApJ, 335, 215
Reach, W. T., & Rho, J. 2000, ApJ, 544, 843
Rho, J., Petre, R., & Hester, J. J. 1993, in The Soft X-ray Cosmos: *ROSAT* Science Symposium, ed. E. M. Schlegel & R. Petre (New York: AIP), 318
Richter, M. J., Graham, J. R., & Wright, G. S. 1995, ApJ, 454, 277
Rieke, G. H., & Lebofsky, M. J. 1985, ApJ, 288, 618
Saken, J. M., Fesen, R. A., & Shull, J. M. 1992, ApJS, 81, 715
Skrutskie, et al. 1997, The Impact of Large-Sscale Near-IR Sky Surveys, ed. F. Garzon et al. (Dordrecht: Kluwer), 25
van Dishoeck, E. F., Jansen, D. J., & Phillips, T. G. 1993, A&A, 279, 541
Wang, Z, & Scoville, N. Z. 1992, ApJ, 386, 158